Usefulness of inclined circular cylinders for designing ultra-wide bandwidth piezoelectric energy harvesters: experiments and computational investigations

Junlei Wang[1], Chengyun Zhang[1], Daniil Yurchenko[2], Abdessattar Abdelkefi[3], Mingjie Zhang[4,*], Huadong Liu[1,]**

[1]School of Mechanical and Power Engineering, Zhengzhou University, Zhengzhou 450000, China;
[2]Institute of Mechanical, Process & Energy Engineering, Heriot-Watt University, Edinburgh EH14 4AS, UK;
[3]Department of Mechanical and Aerospace Engineering, New Mexico State University, Las Cruces, NM 88003, USA;
[4]Department of Structural Engineering, Norwegian University of Science and Technology, 7491, Trondheim, Norway.
[*]Corresponding author: Mingjie Zhang, email address: mingjie.zhang@ntnu.no;
[**]Corresponding author: Huadong Liu, email address: hdliu1984@zzu.edu.cn.

Abstract

This study proposes to change the inclination angle (α) of a circular cylinder with respect to oncoming flow in order to broaden the effective wind speed bandwidth of the piezoelectric energy harvester. Comprehensive wind tunnel experiments are conducted to investigate the energy harvesting characteristics of the system under different inclination angles. The experimental results demonstrate that compared to the conventional vortex-induced vibration piezoelectric energy harvester (VIVPEH), an appropriate inclined cylinder can broaden the effective wind speed range for the VIVPEH. It is experimentally shown that the inclined cylinder at α = 60° can reduce the threshold wind speed and broaden the effective wind speed bandwidth by more than 229%. In addition, inclined circular cylinders at α = 25°, 30°, 35°, 40°, and 45° can produce torsional vibration and high voltage output under high wind speed. Through frequency analysis and computational fluid dynamics (CFD) simulations, the influence mechanism and causes of torsional vibration are explored in detail. The results show that the axial flow will prevent the free shear layer from falling off and cause the force imbalance at the top and bottom of the inclined cylinder, resulting in a torsional vibration and a series of other phenomena. The appearance of the torsional vibration rapidly reduces the frequency of the conventional transverse vortex-induced vibration (VIV). The superposition of the transverse bending vibration and the torsional vibration within a certain wind speed range results in a high voltage output.

Keywords: Piezoelectric energy harvester, inclined circular cylinder, vortex-induced vibration, ultra-wide bandwidth, torsional vibration

1. Introduction

Over recent years, the emergence and application of micro-electro-mechanical systems, health monitoring and wireless sensor networks have promoted the demand for power supplies with high energy density, small size and long working life [1-4]. Micro/nano-scale energy devices that capture renewable energy from the environment have aroused great interest [5-7]. Energy harvesters that convert energy in the environment, such as solar energy, thermal energy, water energy, wind energy, and human movement, into usable electrical energy have been widely developed [8-12]. In particular, wind energy is considered as a clean and environmental-friendly energy source. Hence, wind energy harvesters based on flow-induced vibration (FIV) have attracted more and more attention in recent years [13-16]. According to different FIV mechanisms such as flutter [17,18], vortex-induced vibration (VIV) [19-21], galloping [22,23], and wake galloping [24,25], wind energy can be converted into mechanical/vibration energy. Then the vibration energy is converted into electrical energy through various energy transmission mechanisms including piezoelectric [26], electromagnetic [27], electrostatic [28], and triboelectric [29], etc. Among them, piezoelectric energy harvesters (PEHs) have attracted much attention due to the high voltage output which is easy to design a rectify electrical circuit [30].

As a self-excited aeroelastic instability caused by fluid-structure interaction, VIV is widely used in wind energy harvesting [31,32]. A conventional vortex-induced vibration piezoelectric energy harvester (VIVPEH) can be constructed by attaching a vertical cylinder bluff body to the tip of a piezoelectric cantilever beam. To broaden the effective wind speed bandwidth or improve the efficiency of energy harvesting, numerous theoretical, computational, and experimental studies have been conducted, and various improvement measures have been proposed [33,34]. The common method is to change the aerodynamic cross-section shape of the bluff body and add detachable accessories [35-38]. For example, Wang et al. [39] investigated hybrid piezoelectric wind energy harvesters with different cross-section bluff bodies, which can couple the vibration characteristics of VIV and galloping, thereby greatly reducing the threshold wind speed and enhancing the output voltage. Weinstein et al. [40] installed a movable aerodynamic fin at the end of the piezoelectric cantilever to manually adjust the resonance frequency of VIVPEH, thereby expanding the bandwidth of wind speed. Hu et al. [41] added two small rods on the surface of the bluff body of VIVPEH. Meanwhile, advanced non-linear technology is employed by researchers

to improve the performance of VIVPEH [42]. Zhang et al. [43] innovatively proposed to add a pair of mutually exclusive nonlinear magnetic forces in the VIVPEH device. The results suggested that compared with the conventional configuration, the lock-in region range and energy harvest efficiency of the device are increased by 138% and 29%, respectively. In addition, the piezoelectric-electromagnetic hybrid VIVPEH developed by Zhao et al. [44] realized the combination of vibration piezoelectric and electromagnetic power generation. Experimental results demonstrated that the maximum output power of the device reaches 16.55 mW, which is much higher than the power generation efficiency of conventional single-mode VIVPEH. Furthermore, Franzini and Bunzel [45] explored obtaining energy from VIV with two degrees of freedom (2-DOF) and constructed a 2-DOF VIVPEH model. The results indicated that compared with the conventional 1-DOF VIVPEH, the energy harvesting efficiency can be increased by up to 50% for a particular wind speed.

In all relevant studies cited above, including the modification of aerodynamics, the introduction of nonlinear mechanisms and the realization of multiple degrees of freedom, have increased the extra cost of energy harvester design. on the other hand, the majority of the current researches focused on the structures with their principal axes of the cylinder perpendicular to the wind direction. However, in practical engineering, the direction of incoming flow is not always perpendicular to the axis of the cylinder, and there is usually a certain inclination angle. Inspired by the above, researchers conducted a series of studies on cylinder bluff bodies inclined to the wind direction by simply changing the installation method of the structure itself. For example, Tang et al. [46] used a three-dimensional numerical simulation method to investigate the phenomenon of inclined square cylinder galloping in a smooth flow. It is revealed that Karman vortex shedding mechanism has no significant impact on the galloping oscillation of an inclined cylinder. Recently, Hu et al. [47] performed an interesting experimental study in which square cross-section cylinders inclined at different angles in the wind tunnel have been considered, towards (cylinder with forward inclination) or away (cylinder with backward inclination) from the incoming wind flow. It was found that as the forward inclination angle of the cylinder increased, the corresponding amplitude of the cylinder monotonously decreased. However, when the cylinder inclined backward, there existed an optimum angle to achieve the largest oscillation amplitude. Furthermore, Javed and Abdelkefi [48] conducted theoretical research on understanding the inclined cylinders which

exhibits galloping oscillations but focus on energy harvesting. It can be concluded that a vertical cylinder or a mildly forward inclined cylinder is the best configuration for generating the maximum response. Any high inclination of the square cylinder forward or backward only reduces the vibration response of the cylinder. Unfortunately, to the authors' best knowledge, the energy harvesting of VIV-based inclined cylinders has not been well studied and still lacks of physical explanation to understand the underlying mechanism. In addition, the previous literature has conducted a large amount of theoretical studies on the internal mechanism and characteristics of the VIV-based inclined cylinder. Shirakasi et al. [49] found in wind tunnel tests that the inclination angle caused irregular vortex shedding and reduced vortex shedding frequency, and the vortex shedding frequency gradually decreases with the increase of the inclination angle. And for the first time, the vortex motion in the axial direction on the back of the inclined cylinder was observed, and the depression of vortex shedding frequency was attributed to the secondary flow behind the inclined cylinder. Subsequently, Matsumoto [50] proposed the concept of an axial vortex, and referred to this secondary flow as "axial flow". Furthermore, Hogan and Hall [51] measured the pressure fluctuation curve at different positions of the inclined cylinder and performed a frequency spectrum analysis. They pointed out that when the cylinder inclination angle is large, the Karman vortex street near the top of the cylinder has been completely destroyed. Through the circulating flume experiment, Franzini et al. [52] found that the axial flow behind the cylinder will have a certain impact on the interaction between the free shear layers on the cylinder surface. Moreover, with the increase of the inclination angle of the cylinder, the vortex shedding mechanism becomes more and more irregular. Nevertheless, there is still a lack of research on energy harvesting of VIV-based inclined cylinders.

In summary, although there have been several theoretical/experimental studies on inclined cylinders, there are few studies on VIVPEH based on inclined cylinder bluff bodies. Inspired by the aforementioned studies, this investigation proposes to change the inclination angle α from a vertical circular cross-section cylinder to obtain inclined cylinder bluff bodies with different inclination angles to broaden the wind speed bandwidth of conventional VIVPEH. In this study, nine different inclination angles α (0°, 25°, 30°, 35°, 40°, 45°, 50°, 55°, and 60°) are experimentally tested in a wind tunnel for the performance evaluation. In section 2, the design concept and experimental setup of the proposed energy harvesters are introduced. Section 3 comprehensively

analyzes and discusses the experimental results under different inclination angles. Moreover, taking the inclined cylinder at α = 25° as an example, the causes of the "two humps" phenomenon is analyzed in detail, and the influence mechanism between transverse bending and torsional modes of vibration is discussed through frequency analysis. In Section 4, three-dimensional computational fluid dynamics (CFD) simulations results are used to illustrate the mechanism and causes of the torsional vibration. Section 5 concludes the key findings.

2. Design concept and experimental setup

In this section, the design concept and the manufactured prototypes of the proposed energy harvesters are first introduced, and then the overall environment of the wind tunnel experiment is described. As shown in Fig. 1(a), a typical VIVPEH is composed of a circular cylinder bluff body, a cantilever beam, and a piezoelectric transducer bonded at the root of the beam. In general, when the airflow above the threshold speed passes through a cylinder supported on a cantilever beam, the cylinder will be subjected to unsteady aerodynamic forces, which will activate the vibration of the beam and lead to power generation by the piezoelectric transducer. The conventional VIVPEH usually employs a vertical cylinder as the bluff body, that is, the cylinder and the cantilever beam present a T-shaped structure and are perpendicular to the windward direction. By changing the inclination angle α from the vertical cylinder, inclined cylinders with different inclination angles can be obtained. Inclined cylinders with different inclination angles may bring different aerodynamic characteristics and possible activation of the torsional mode of the structure. Therefore, it is worth to investigate the influence of inclination angle α on the performance of energy harvester. In this study, nine different inclination angles α (0°, 25°, 30°, 35°, 40°, 45°, 50°, 55°, and 60°) are investigated and discussed. It should be noted that for performance comparison, the conventional VIVPEH using a vertical cylinder at α = 0° is also presented. Fig. 1(b) - (e) present the photos of the piezoelectric energy harvester prototype with cylinders at α = 0°, 30°, 45°, and 60°. In all cases, the same cylinder bluff body made of rigid foam is employed, with a height of H = 120 mm and a diameter of D = 32 mm. The cantilever beam material is aluminum, with dimensions of $L \times W \times h_b$ = 200 × 25 × 0.5 mm^3, where L, W, and h_b are the length, width, and thickness of the beam, respectively. The piezoelectric transducer is made of PZT-5 material (internal capacitance is 23.3 nF), which is bonded at the root of the cantilever beam. The entire piezoelectric energy harvesting system is fixed on a stable aluminum frame.

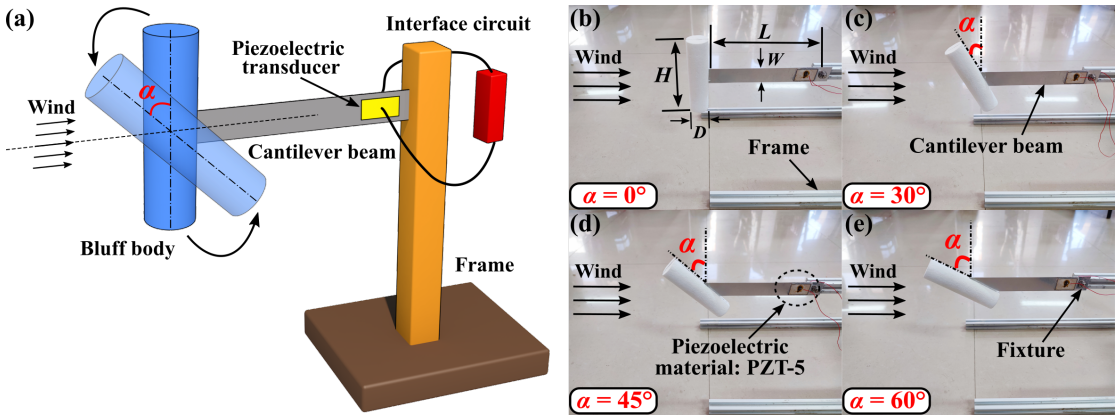

Fig. 1. The design concept and prototypes of proposed energy harvesters: (a) the principle of the piezoelectric energy harvester and (b)-(e) the photos of the piezoelectric energy harvester prototypes with circular cylinders at α = 0°, 30°, 45°, and 60°.

To test the effectiveness of the proposed energy harvesters, this study conducts comprehensive wind tunnel experiments. Fig. 2 presents the overview of the entire wind tunnel experimental setup. The experiments are conducted in an open-circuit circular-section wind tunnel. The length and diameter of the wind tunnel are 5 m and 0.4 m respectively. There are two stages of honeycomb-like structure inside to form a stable section to ensure the uniformity and stability of the incoming wind flow. The energy harvester shown in Fig. 1(b) - (e) is installed in the test section of the wind tunnel. By adjusting the speed of the draft fan, the wind speed of the wind tunnel can be controlled. The wind speed is measured by a hot wire anemometer (Testo Co., USA), and the tested wind speed range is U = 1.00 m/s ~ 6.48 m/s. The voltage signal generated by the piezoelectric transducer and the displacement signal of the bluff body are recorded by a dual-channel digital oscilloscope (ISDS220B) and a laser displacement sensor (Panasonic: HG - C1400), respectively. It should be noted that for each wind speed, the long-term time history responses of the voltage and displacement of the bluff body in steady-state vibration are recorded. The RMS value of voltage (V_{rms}) and the maximum value of the displacement (y_{max}) are then calculated accordingly. The output power is determined by the following relation V_{rms}^2/R, where R denotes the electrical load resistance in the connected circuit.

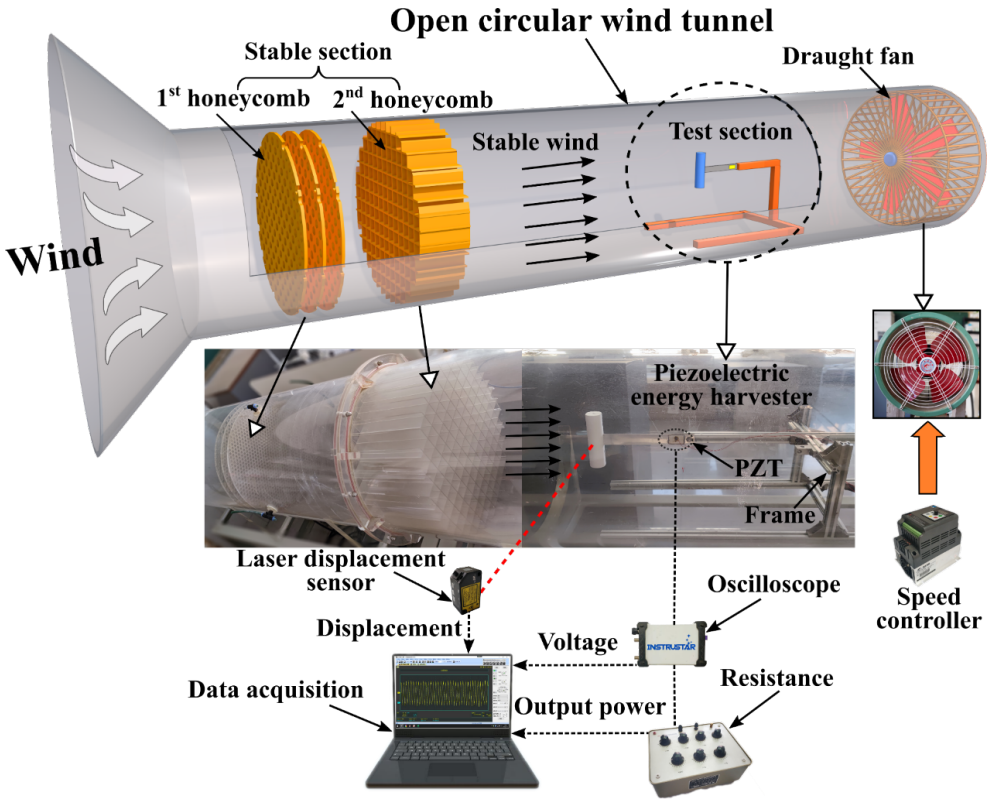

Fig. 2. The wind tunnel experiment setup.

3. Experimental results and discussion

3.1. Comprehensive analysis of the inclined cylinder at $\alpha = 25°$

This subsection first compares the the voltage output and vibration response of the energy harvester with an inclined cylinder at $\alpha = 25°$ and a conventional vertical cylinder. Then, the causes of the "two humps" phenomenon is analyzed in detail, and the influence mechanism between transverse bending and torsional modes of vibration is discussed through frequency analysis. Fig. 3(a) and (b) present the performance comparison of energy harvesters with the circular cylinder at $\alpha = 0°$ and $\alpha = 25°$. From Fig. 3(a), one can see that the energy harvester with the inclined cylinder at $\alpha = 25°$ has a lower threshold wind speed than the energy harvester with the circular cylinder at $\alpha = 0°$ (conventional VIVPEH). Moreover, when the wind speed is higher than 3.19 m/s, the VIV of the cylinder at $\alpha = 0°$ elapses, resulting in no voltage output. In contrast, the vibration of the inclined cylinder at $\alpha = 25°$ still exists, which continuously produces a larger voltage output. Interestingly, it can be seen that the inclined cylinder at $\alpha = 25°$ has two humps phenomena within the investigated range of wind speeds. These phenomena occur because of the coupling between the transverse bending and torsional modes of vibration of the inclined cylinder at high wind speeds, which will be interpreted in the following section in detail. The wind speed bandwidth of the first

hump and the second hump are U = 1.41 m/s ~ 4.02 m/s and U = 4.02 m/s ~ 6.48 m/s, respectively. However, the wind speed bandwidth of the inclined cylinder at $\alpha = 0^{\circ}$ is U = 1.69 m/s ~ 3.19 m/s, which is far less than the working wind speed range when the inclined cylinder at α = 25°. In addition, the maximum RMS voltage output of the first and second hump of the inclined cylinder at α =25° reaches 4.63 V and 2.55 V, respectively, which is lower than the maximum voltage of 5.44 V that can be obtained by the conventional circular cylinder at α = 0°. The plotted curves in Fig. 3(b) presents the maximum displacement comparison of energy harvesters with the circular cylinder at α = 0° and α = 25°. It follows from this figure that the maximum displacement and generated voltage present the same trend. Similarly, the maximum displacement of the inclined cylinder at α = 25° has the phenomena of two humps, and it has lower threshold speed and wider wind speed bandwidth, but smaller displacement compared with the cylinder at α = 0°. This is consistent with the results studied by Shirakasi et al. [49], that is, the inclination angle may cause a decrease in the frequency of vortex shedding, which reduces the aerodynamic force received by the inclined cylinder, and thus leads to a decrease in the generated voltage and tip displacement of the energy harvester. In summary, compared with the conventional VIVPEH, the piezoelectric energy harvester with the inclined circular cylinder at α = 25° greatly improves the wind speed bandwidth and reduces the threshold wind speed, but the maximum voltage and displacement are slightly reduced. Therefore, this characteristic of the energy harvester with the inclined circular cylinder at α = 25° is suitable for low power sensor devices which are insensitive to voltage output but require larger wind speed bandwidth.

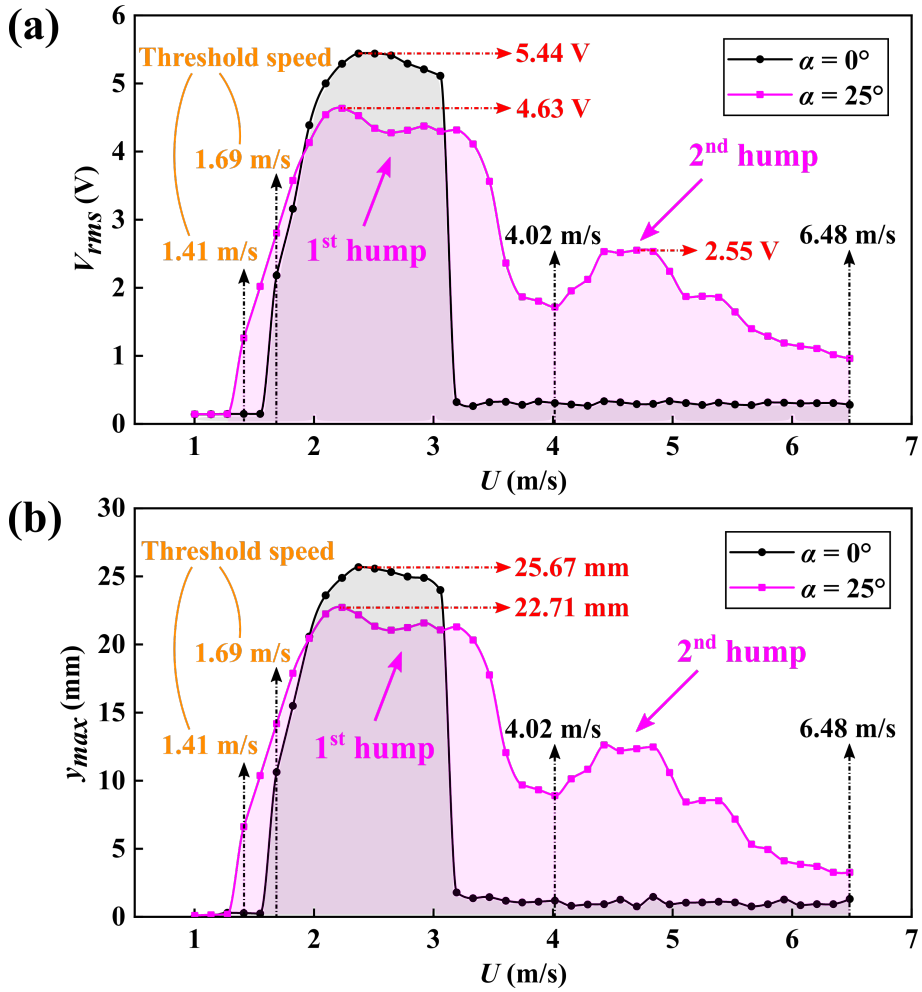

Fig. 3. Performance comparison between the energy harvester with the circular cylinder at $\alpha = 0°$ and $\alpha = 25°$: (a) RMS voltage output and (b) maximum displacement of the bluff body.

To explain the two humps phenomena of the inclined cylinder at $\alpha = 25°$ shown in Fig. 3, Fig. 4 presents the representative voltage time-histories (0 - 30 s in length) of the inclined cylinder at $\alpha = 25°$. It can be found that when the wind speed is 1.41 m/s, 2.24 m/s, and 2.92 m/s, the amplitude of the voltage at each wind speed hardly changes with time, and the envelope of the generated voltage is almost straight. At this time, the bluff body is in a relatively stable single-frequency periodic oscillation due to the transverse bending. When the wind speed reaches 4.02 m/s, 4.70 m/s, and 6.48 m/s, the voltage signal at each wind speed has an obvious “beat” phenomenon, that is, the voltage amplitude exhibits a periodic change over time. Meanwhile, the envelope of voltage signal fluctuates periodically, which indicates that the bluff body is in the periodic oscillation state of superposition of multiple frequencies.

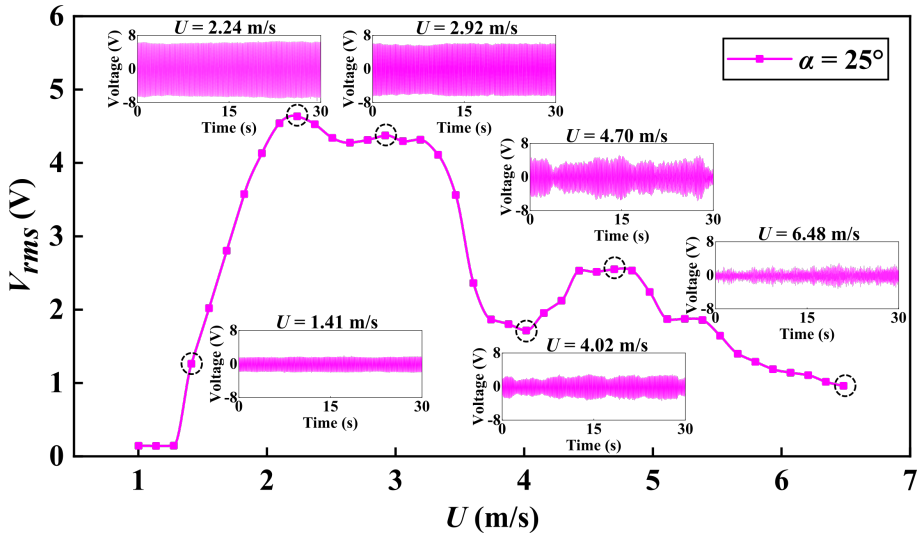

Fig. 4. The representative time-histories of voltages of the inclined cylinder at $\alpha = 25°$.

To further investigate the phenomenon of frequency superposition, Fig. 5(a) and (b) present the time-domain (0 - 1s) and frequency-domain curves of voltages at representative wind speeds of the inclined cylinder at $\alpha = 25°$. One can see that when the wind speed is equal to 1.41 m/s, 2.24 m/s, and 2.92 m/s, the voltage signal fluctuates periodically with time, and only one frequency appears in its spectrum, which indicates that the current wind speed is in the process of conventional VIV. However, when the wind speed reaches 4.02 m/s, a high-frequency harmonics of 35.21 Hz appears, which is the threshold wind speed resulting in the high frequency. In addition, due to the small voltage amplitude of higher frequency, the voltage amplitude superimposed by frequency has a small change. Afterward, when the wind speed reaches 4.70 m/s and 6.48 m/s, the amplitude of higher frequency is significantly larger than that of U = 4.02 m/s, and an obvious frequency superposition phenomenon can be observed on the time-history of the voltage curve. It is worth noting that when $U < 4.02$ m/s, the voltage amplitude of the lower frequency rises first and then drops as the wind speed increases, so it is regarded as a conventional VIV process. And when $U >$ 4.02 m/s, with the introduction of higher frequency, the voltage amplitude of the lower frequency rises and then drops again, resulting in the second hump phenomenon. Therefore, it can be concluded that the first hump of the inclined cylinder at $\alpha = 25°$ is a conventional VIV with a broadened wind speed bandwidth, while the second hump is caused by the introduction of a higher frequency harmonics.

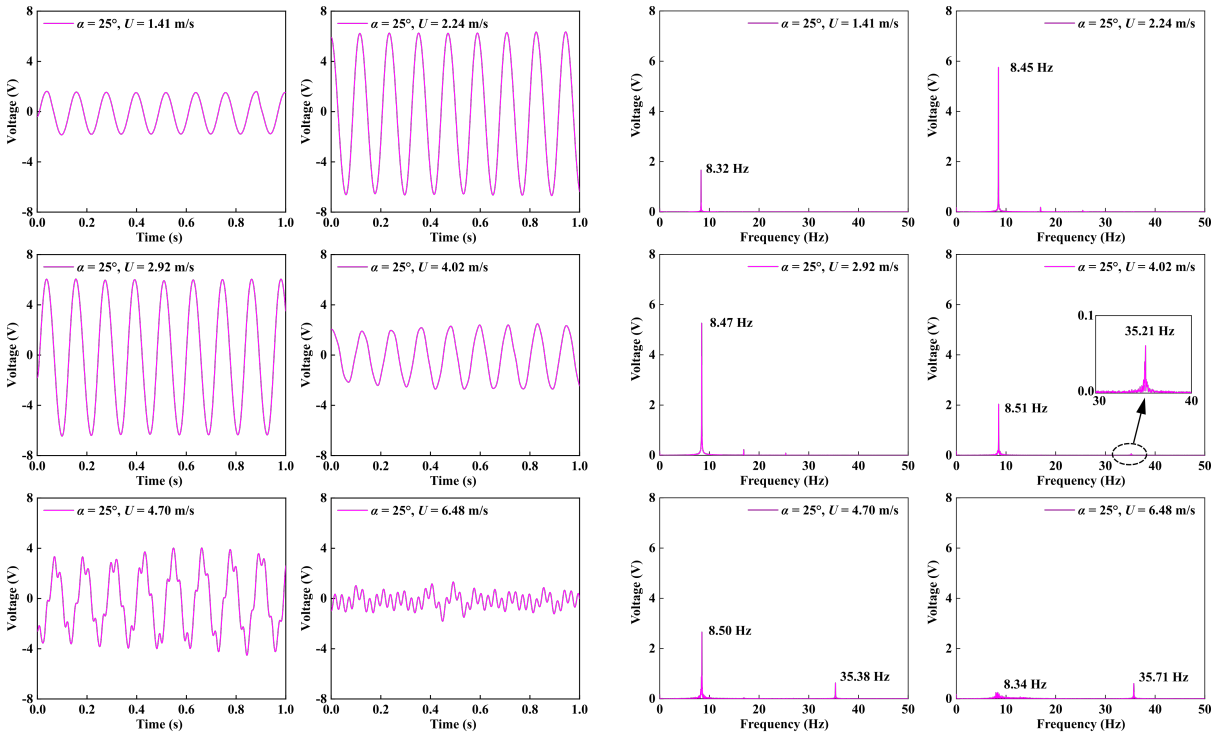

Fig. 5. Time-domain and frequency-domain curves of voltages at representative wind speeds of the inclined cylinder at $\alpha = 25°$: (a) the time-history responses (0 - 1s) and (b) the associated frequency spectra.

To better understand the vibration mode of the higher frequency in the second hump, Fig. 6(a) and (b) present two vibration modes of the bluff body observed in the experiment. One can see that the transverse bending vibration mode is a translational movement, that is, the upper and lower ends of the bluff body move in parallel in the same direction. However, in the torsional vibration mode, the upper and lower ends of the bluff body move in opposite directions, which leads to the torsion of the beam connected with the bluff body and the torsional deformation of the piezoelectric sheet attached to the end of the beam, resulting in output voltage. It is worth noting that the laser spot of the laser displacement sensor hits the center of the bluff body when measuring displacement, which means that when torsional vibration occurs, a large voltage can be collected, but the measured transverse displacement may be negligible. In this study, beam and bluff body are not connected by a conventional joint or a hinge. Fig. 6(c) and (d) show the downwind cross-section schematic diagrams of bluff body attached to the beam. The insertion area of the beam and the constraint length may affect the torsion of the inclined cylinder. As the inclination angle increases, the constraint length of the inserted beam gradually increases, which will make it more and more difficult for the inclined cylinder to twist, which will change the torsional mode natural frequency.

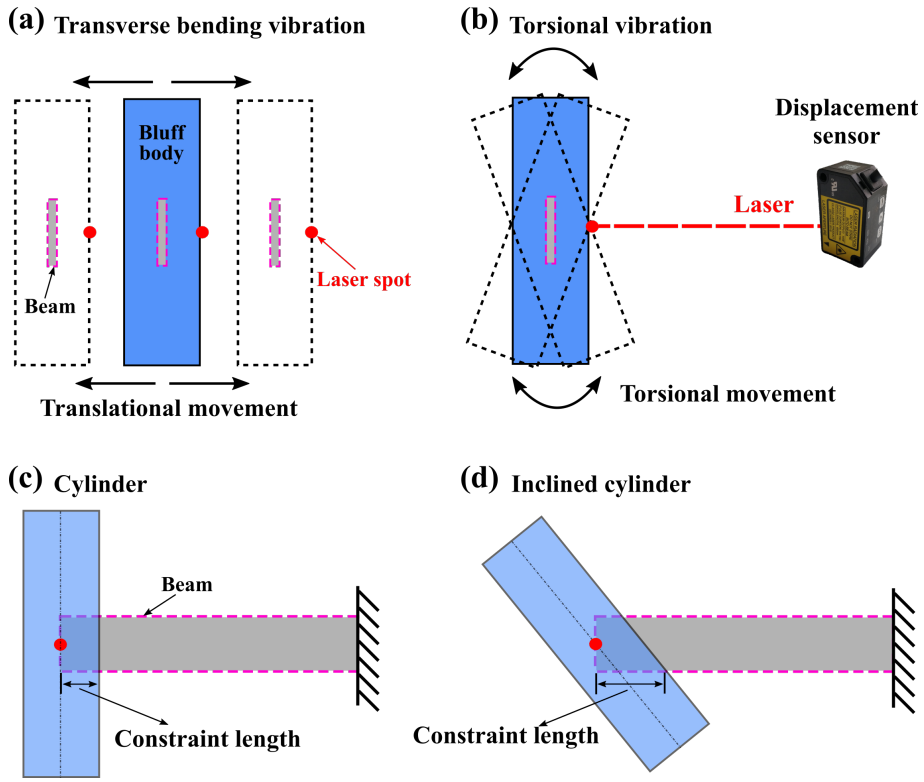

Fig. 6. The windward cross-section schematic diagrams of: (a) transverse bending vibration mode and (b) torsional vibration mode of bluff body observed in the experiment; the downwind cross-section schematic diagrams of (c) cylinder and (d) inclined cylinder bluff body attached to the beam.

To prove that the higher frequency in the second hump is the torsional vibration of Fig. 6(b), the torsional free decay test is done on the inclined cylinder at $\alpha = 25°$. It should be noted that the transverse free decay test is to make the bluff body performing the translational movement shown in Fig. 6(a) during the entire process of free decay. In contrast, the torsional free decay test is to keep the bluff body vibrating in the torsion state, as shown in Fig. 6(b), and then perform the free decay test, so that the transverse bending vibration and torsional vibration modes will appear simultaneously during the entire process. Fig. 7(a) and (b) present the voltage time-history curves and corresponding FFT results of the transverse and torsional free decay tests of the inclined cylinder at $\alpha = 25°$. It can be seen that there is a fundamental frequency of 8.48 Hz in the transverse free decay test, while there are two frequencies of 8.46 Hz and 35.15 Hz in the torsional free decay test. Therefore, it can be concluded that the lower fundamental frequency in Fig. 7(b) is the transverse bending natural frequency and the higher fundamental frequency is the torsional natural frequency. Furthermore, the higher frequency in the voltage spectrum shown in Fig. 5(b) is close to the torsional natural frequency, so it can be concluded that the inclined cylinder at $\alpha = 25°$ has high-frequency torsional vibration at high wind speed. It is also worth noting that the transverse

bending natural frequencies obtained from both the transverse and torsional free decay tests are almost the same. As a comparison, Fig. 7(c) depicts the results of the transverse free decay test of the cylinder at $\alpha = 0°$. The transverse bending natural frequency is insignificantly affected by the incline angle. However, the torsional mode is not excited for the cylinder at $\alpha = 0°$ in the wind tunnel experiment due to the symmetric wind loads.

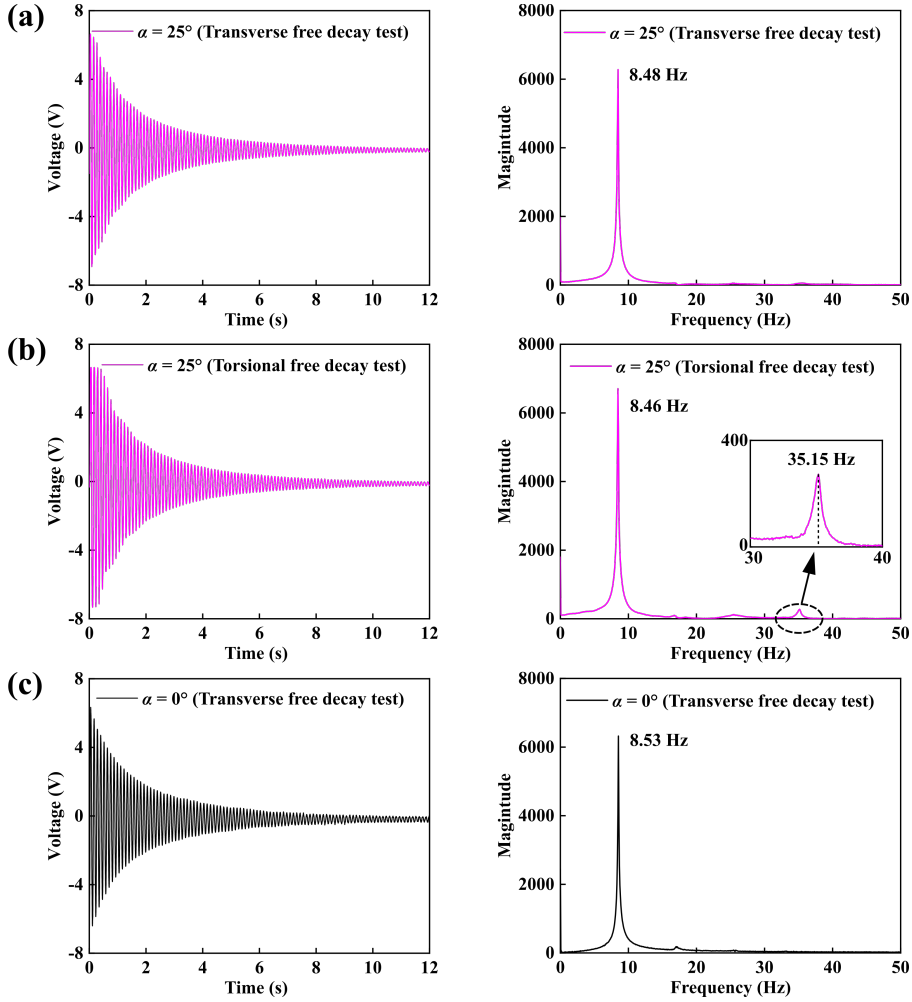

Fig. 7. Voltage time-history curves and corresponding FFT results of free decay tests: (a) transverse free decay test at $\alpha = 25°$, (b) torsional free decay test at $\alpha = 25°$, and (c) transverse free decay test at $\alpha = 0°$.

To analyze the interaction of the two vibration modes in the experiment, Fig. 8(a) and (b) demonstrate the variation of the dimensionless vibration frequency versus the wind speed for cylinders at $\alpha = 0°$ and $\alpha = 25°$. It should be noted that the dimensionless frequency f_c / f_{cn} is the ratio of the transverse bending vibration frequency and the transverse bending natural frequency. Similarly, f_t / f_{tn} is the ratio of the torsional vibration frequency and the torsional natural frequency. f_c and f_t are obtained from the voltage time-history by the FFT method, that is, the vibration frequency of the bluff body is assumed to consistent with the fluctuation frequency of the voltage.

f_{cn} and f_{tn} are obtained from the torsional free decay test of the cylinder. As the wind speed increases, two branches of the cylinder at $\alpha = 0°$, which are the initial excitation branch and the lower branch, can be observed in Fig. 8(a). However, the upper branch (lock-in region), which is one of the three typical regions of VIV, has not been observed due to the high mass ratio [53]. In Fig. 8(b), three typical regions of VIV can be observed. The dimensionless frequency f_c / f_{cn} increases gradually with the increase of wind speed in the initial excitation branch region of VIV, and then maintains near 1 in the upper branch region (lock-in region). As the wind speed further increases to the lower branch region of VIV, the dimensionless frequency f_c / f_{cn} increases rapidly again. It is worth noting that the effective wind speed bandwidth of the transverse vibration region of the inclined cylinder at $\alpha = 25°$ is 1.41 m/s ~ 4.02 m/s, which is 90.51% wider than that of the cylinder at $\alpha = 0°$ (i.e. [(4.02 - 1.41) - (3.06 - 1.69)] / (3.06 - 1.69) × 100%).

Moreover, compared to the cylinder at $\alpha = 0°$ with only transverse bending vibration, the inclined cylinder at $\alpha = 25°$ begins to exhibit torsional vibration when the wind speed is 4.02 m/s. In the coupled vibration region, the dimensionless frequency f_t / f_{tn} of torsional vibration increases almost linearly with the increase of wind speed. Interestingly, the appearance of torsional vibration has caused a decrease in f_c / f_{cn} that should have been rising all the time after the lock-in region of VIV. When the wind speed is in the range of 4.02 m/s ~ 5.11 m/s, the dimensionless frequency f_c / f_{cn} and f_t / f_{tn} are both around 1, indicating that the transverse bending vibration frequency and the transverse bendingnatural frequency are synchronized again, and the torsional vibration frequency and the torsional natural frequency are also synchronized. Therefore, the transverse bending vibration of the bluff body produces a larger oscillation amplitude, while the torsional vibration produces a larger torsional amplitude and brings a larger strain to the piezoelectric cantilever. Finally, under the combined action of the transverse bending vibration and torsional vibration, the energy harvester produces high voltage output. When $U > 5.11$ m/s, the torsional vibration frequency gradually increases as the wind speed increases, which is accompanied by a gradual decrease in the transverse bending vibration frequency. Therefore, f_c / f_{cn} and f_t / f_{tn} are both far away from 1, and the transverse bending vibration and torsional vibration responses both enter the desynchronization, which results in a decrease in the generated voltage. According to the above analysis of frequency, the reason for the formation of the second hump is explained.

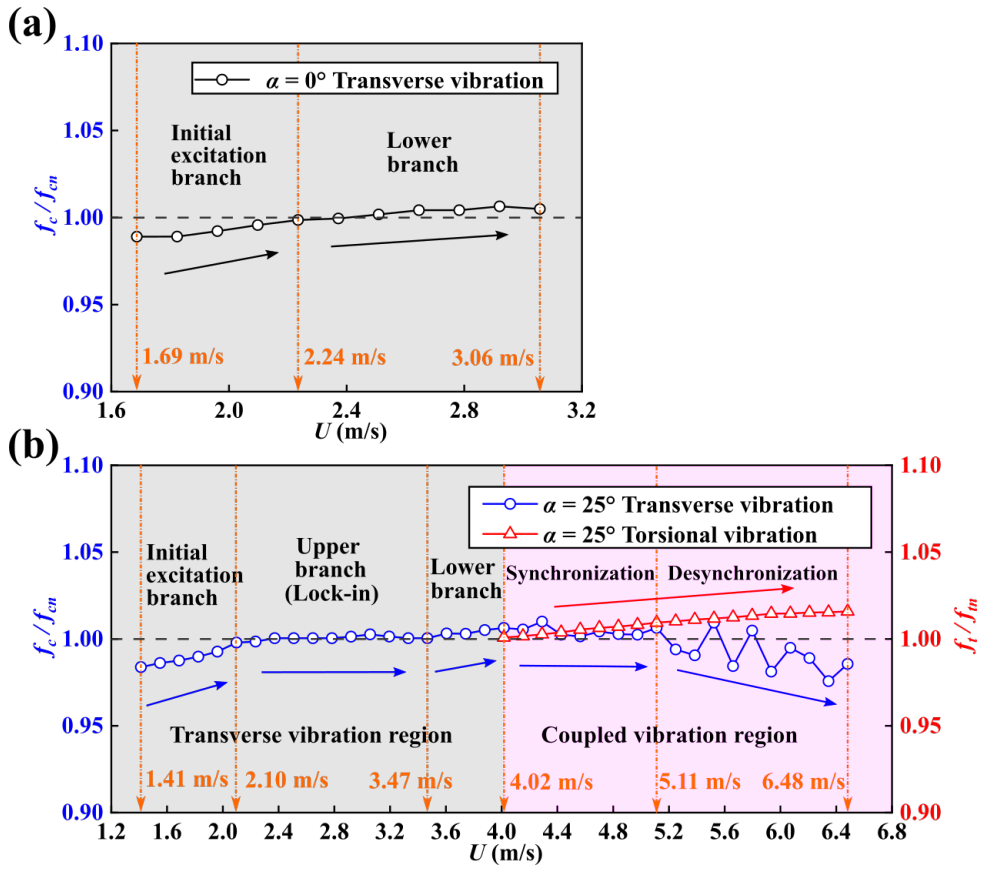

Fig. 8. Variation of the dimensionless vibration frequency versus wind speed: (a) $\alpha = 0°$ and (b) $\alpha = 25°$.

3.2. Performance comparison of inclined cylinders at $\alpha = 25° \sim 40°$

In this subsection, the performance of the energy harvesters with inclined circular cylinders at $\alpha = 25° \sim 40°$ is compared, and the comprehensive frequency analysis further reveals the interaction mechanism between the transverse bending vibration and torsional vibration. The plotted curves in Fig. 9 show the performance comparison between the piezoelectric energy harvesters with circular cylinders at $\alpha = 25° \sim 40°$ and $\alpha = 0°$. It can be seen that the threshold wind speed of the inclined cylinder at $\alpha = 25°$, 30°, 35°, and 40° is 1.41m/s, which is lower than the threshold wind speed of 1.69 m/s of the cylinder at $\alpha = 0°$. In general, the wind speed bandwidth of the VIV region (the first hump) increases with the increase of inclination angle α of the inclined cylinder, while the maximum RMS voltage and displacement in the VIV region decrease gradually. Similar to the cylinder at $\alpha = 25°$, the inclined cylinders at $\alpha = 30°$, 35°, and 40° also have the second hump. However, with the increase of angle α, the position of the second hump shifts towards higher wind speed, which means that the threshold wind speed of torsional vibration increases gradually. It should be mentioned that the second hump for the cylinder at $\alpha = 35°$ can produce a higher voltage than that for the cylinder at $\alpha = 30°$, but the displacement of the cylinder at $\alpha = 35°$ is less than that

of α = 30°. In addition, within the investigated range of wind speeds, the second hump with α = 40 ° is in a rising phase and can produce higher voltage, but its displacement is extremely small.

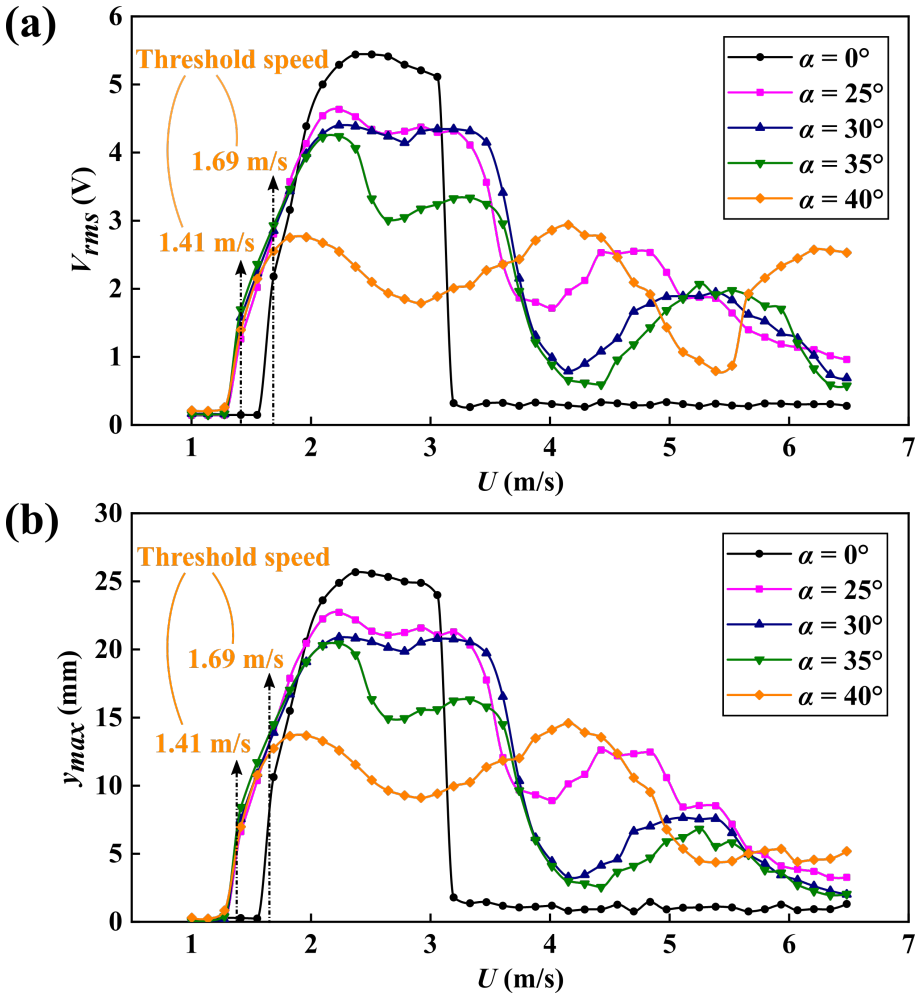

Fig. 9. Performance comparison between the energy harvesters with cylinders at α = 0°, 25°, 30°, 40°: (a) RMS voltage output and (b) maximum vibration displacement of the bluff body.

Fig. 10(a) - (c) present the FFT results of torsional free decay responses of inclined cylinders at α = 30°, 35°, and 40°, and the corresponding variation of the dimensionless vibration frequency versus wind speed. One can see that the torsional natural frequencies of cylinders at α = 30°, 35°, and 40° are 35.22 Hz, 37.47 Hz, and 38.61 Hz, respectively, which indicates that the torsional natural frequencies increase with the increase of angle α. According to the corresponding dimensionless frequency diagram, the threshold wind speed of torsional vibration is gradually increased with the increase of angle α. In detail, the threshold wind speeds of cylinders at α = 30°, 35°, and 40° are 4.15 m/s, 4.43 m/s, and 4.98 m/s, respectively. Therefore, it can be concluded that when the threshold wind speed of the torsional vibration is reached, the torsional vibration frequency of the bluff body is close to the torsional natural frequency and then enters a

synchronized state, which causes the torsional vibration to produce a larger torsional amplitude. In addition, compared with the cylinder at α = 25°, it can be more clearly seen that, for cylinders at α = 30°, 35°, and 40°, the appearance of torsional vibration rapidly reduces the frequency of the transverse bending vibration, then making the transverse bending vibration enter the synchronization region again. Finally, the synchronous region of the transverse bending vibration and torsional vibration superposed in a certain same wind speed range, which causes the voltage to increase rapidly. Besides, as the wind speed keeps increasing, the frequency of torsional vibration continues to increase, and the frequency of transverse bending vibration continues to decrease, and then both of them enter the desynchronization region, resulting in the voltage reduction.

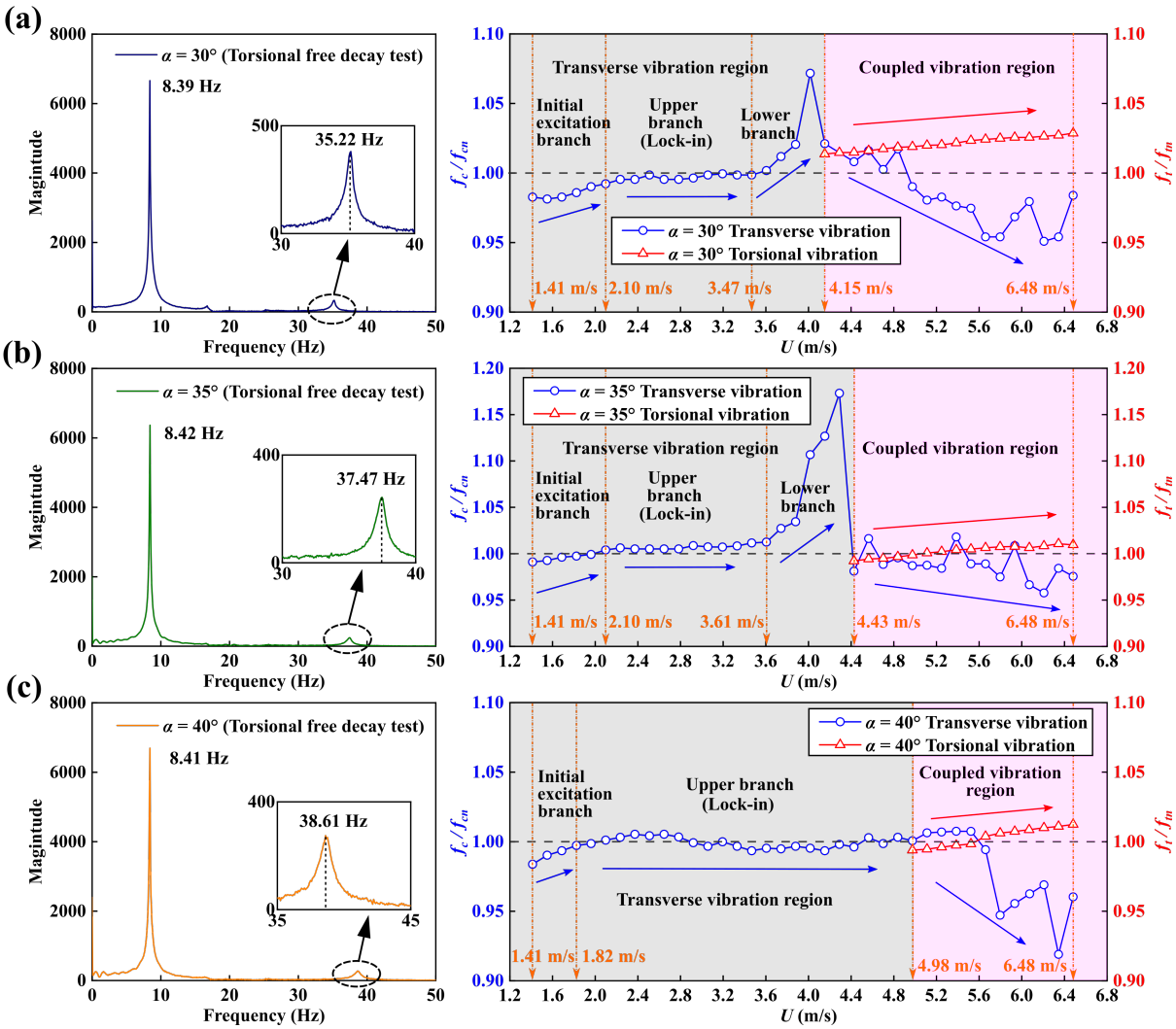

Fig. 10. FFT results of torsional free decay responses of inclined cylinders at different inclination angles and corresponding variation of the dimensionless vibration frequency versus wind speed: (a) α = 30°, (b) α = 35°, and (c) α = 40°.

To further analyze the interaction between the transverse bending vibration and torsional

vibration in the coupled vibration region, Fig. 11(a) - (d) present the frequency spectra of the inclined cylinders at α = 25°, 30°, 35°, and 40°. On the whole, it can be seen that with the increase of the inclination angle α, the dominant vibration mode gradually changes from the transverse bending mode to the torsional mode, that is, the generated voltage amplitude of the transverse bending vibration gradually decreases, while the torsional vibration amplitude gradually increases. In detail, it can be seen from Fig. 11(a) that the voltage amplitude of transverse bending vibration is significantly greater than that of torsional vibration when the wind speed is 4.02 m/s ~ 5.11 m/s, indicating that the circular cylinder α = 25° performs vibrations dominated by transverse bending vibration. Moreover, the voltage amplitudes of the cylinder at α = 25° for both transverse bending vibration and torsional vibration first increase and then decrease with the increase of wind speed. When the wind speed is 4.02 m/s ~ 5.11 m/s, the transverse bending vibration, and torsional vibration can both produce higher voltage, which corresponds to the synchronous region shown in Fig. 8(b). As shown in Fig. 11(b) and (c), cylinders at α = 30° and 35° perform vibrations dominated by torsional mode. However, compared with the cylinder at α = 30°, the amplitude of torsional vibration for the cylinder at α = 35° is higher, and the proportion of torsional vibration is larger. Therefore, it can be used to explain that the observation in Fig. 9: the second hump for the cylinder at α = 35° can produce a higher voltage than that for the cylinder at α = 30°, but the displacement of the cylinder at α = 35° is less than that of α = 30°. In particular, as seen from Fig. 11(d), the cylinder at α = 40° performs vibrations completely dominated by torsional mode. The voltage generated by the transverse bending vibration is extremely small, and its higher voltage output is almost entirely generated by torsional vibration. As a result, the second hump of the cylinder at α = 40° as shown in Fig. 9 can generate a higher voltage, but its displacement is extremely small.

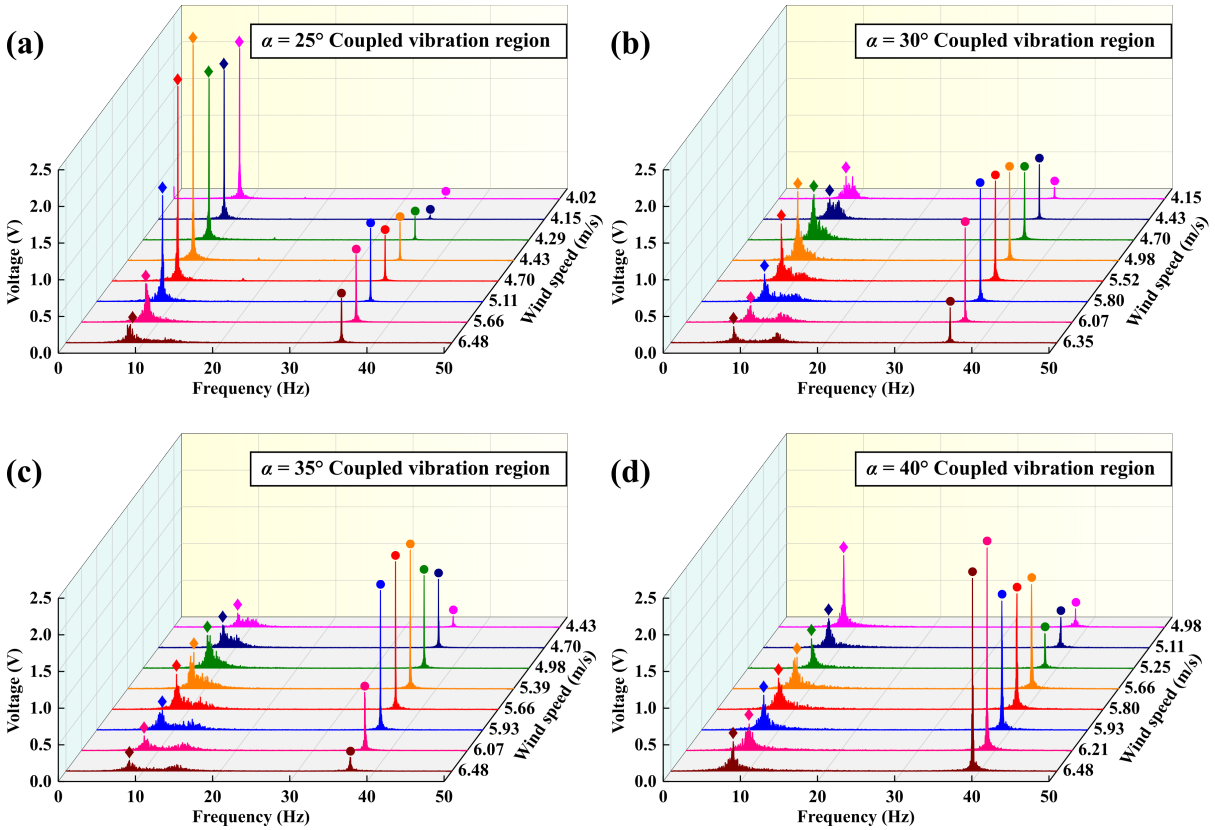

Fig. 11. Frequency spectrum of the coupled vibration region of the inclined cylinder at different inclination angles: (a) $\alpha = 25°$, (b) $\alpha = 30°$, (c) $\alpha = 35°$, and (d) $\alpha = 40°$.

3.3 Performance comparison of inclined cylinders at $\alpha = 45° \sim 60°$

In this subsection, the performance of the energy harvesters with inclined circular cylinders at $\alpha = 45° \sim 60°$ is compared, and the conditions of torsional vibration are further revealed. Fig. 12 shows the performance comparison of the energy harvesters with inclined cylinders at $\alpha = 45° \sim 60°$. Compared with $\alpha = 25° \sim 40°$, when $\alpha > 40°$, continuing to increase the inclination angle α cannot significantly broaden the effective wind speed bandwidth. In addition, as α increases, the threshold wind speed gradually increases. Specifically, the threshold wind speed for $\alpha = 45°$ and 50° is around 1.41 m/s, and the threshold wind speed for $\alpha = 55°$ and 60° is around 1.55 m/s. The inclined cylinder at $\alpha = 60°$ has the widest effective wind speed bandwidth of 1.55 m/s ~ 6.07 m/s, which is 229.93% wider than that of the cylinder at $\alpha = 0°$ (i.e. [(6.07 - 1.55) - (3.06 - 1.69)] / (3.06 - 1.69) × 100%). It should be noted that the overall behaviors for cylinders at $\alpha = 45°$ and $\alpha = 40°$ are similar, i.e., both appear in the rising phase of the second hump. After the end of the first hump, the voltage curve has a short rise, but there is only a very small displacement. In particular, when $\alpha = 50°$, 55°, and 60°, only the first hump appeared, while the second hump was not observed in the considered wind speed range.

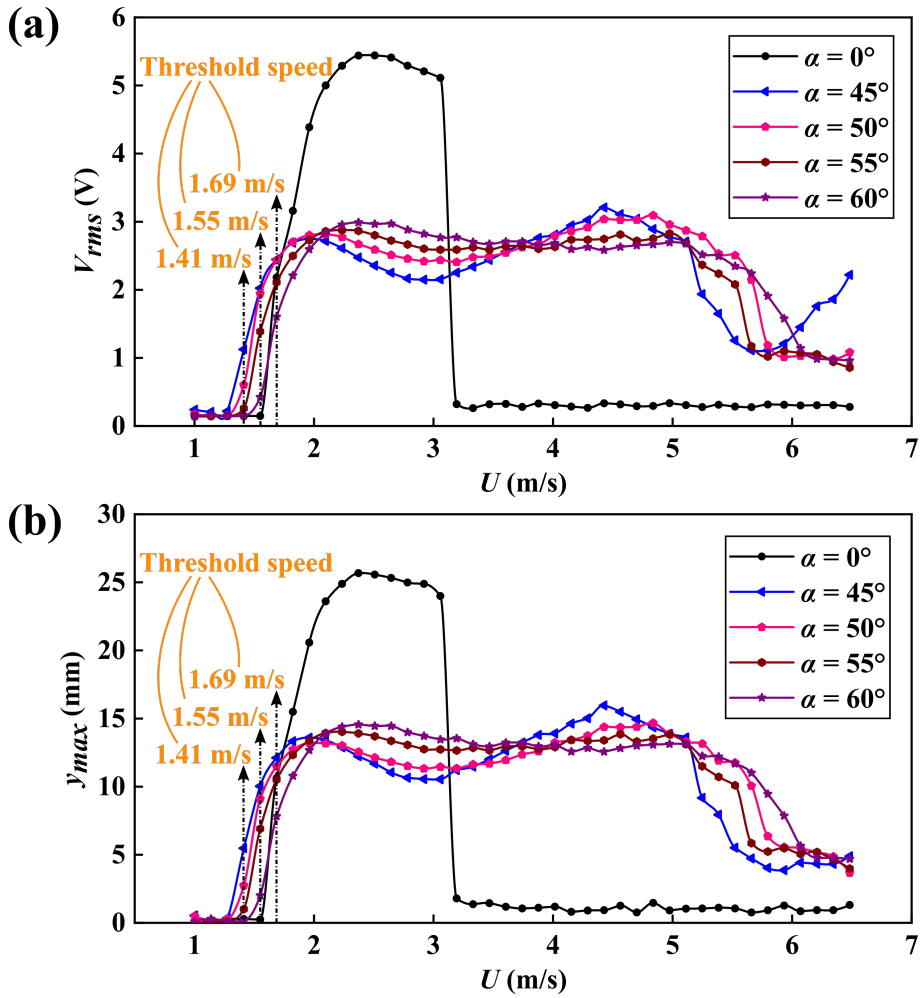

Fig. 12. Performance comparison between the energy harvesters with inclined cylinders at α = 0°, 45°, 50°, 55°, 60°: (a) RMS voltage output and (b) The maximum vibration displacement of the bluff body.

Fig. 13(a) - (d) present the FFT results of the torsional free decay responses of inclined cylinders at α = 45°, 50°, 55°, and 60°. It can be seen that the torsional natural frequencies of cylinders at α = 45°, 50°, 55°, and 60° are 40.85 Hz, 42.15 Hz, 44.92 Hz, and 46.55 Hz, respectively, which are considerably higher than that for cylinders at α = 25° ~ 40°. The torsional natural frequency gradually increases with the increase of the inclination angle α. When α = 50°, 55°, and 60°, the current wind speed cannot induce torsional vibration of the bluff body due to the high torsional natural frequency and the small arm of the flow-induced forces. They may have torsional vibration at higher wind speed, which needs further research in the future.

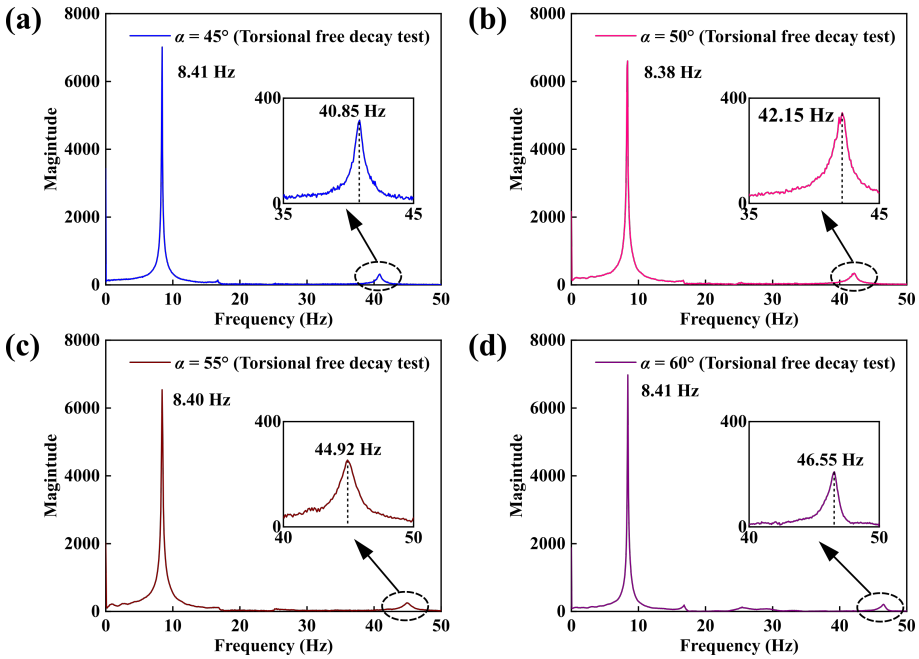

Fig. 13. FFT results of torsional free decay responses of inclined cylinders at different inclination angles: (a) $\alpha = 45°$, (b) $\alpha = 50°$, (c) $\alpha = 55°$, and (d) $\alpha = 60°$.

3.4. Impacts of the inclined cylinder on the optimal performance of the harvester

As known that there exits an optimal electrical load resistance at which the energy harvester has the maximum output power. This subsection explores the impacts of the inclined cylinder on the optimal performance of the energy harvester. Fig. 14(a) presents the power output versus the electrical load resistance for the circular cylinder at $\alpha = 0°$ at different wind speeds. Fig. 14(b) shows the power output versus load resistance for different inclined cylinders at $U = 2.37$ m/s. It can be seen that as the load resistance increases, the power output first increases and then decreases. For all the cases, the power output reaches the maximum value when $R = 0.8$ MΩ. The results indicate that the optimal load resistance obtained from the wind speed range of the transverse vibration region is the same in all cases. In summary, it can be concluded that the R_{opt} depends on the primary structure, and $R = 0.8$ MΩ is selected as the load resistance in this experiment.

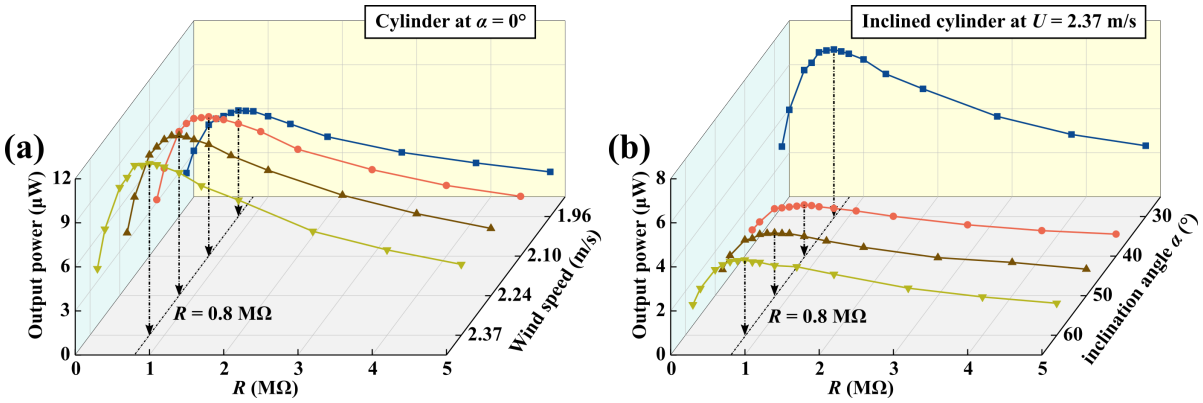

Fig. 14. Variation of the power output against load resistance: (a) power output versus load resistance for the cylinder at $\alpha = 0°$ at different wind speeds and (b) power output versus load resistance for different inclined cylinders at $U = 2.37$ m/s.

The plotted curves in Fig. 15 depict the variation of the harvested power under load resistance ($R = 0.8$ MΩ) against wind speed for different cylinders. It should be mentioned that the variations of the power and voltage versus wind speed are basically the same. Compared with the conventional vertical cylinder bluff body ($\alpha = 0°$), the inclined cylinder can significantly broaden the effective wind speed bandwidth of the energy harvester. However, the maximum power output is reduced by the inclination angle. Therefore, the energy harvester with the inclined cylinder bluff body is suitable for low-power sensor equipment that requires a large effective wind speed bandwidth but does not require a very large power.

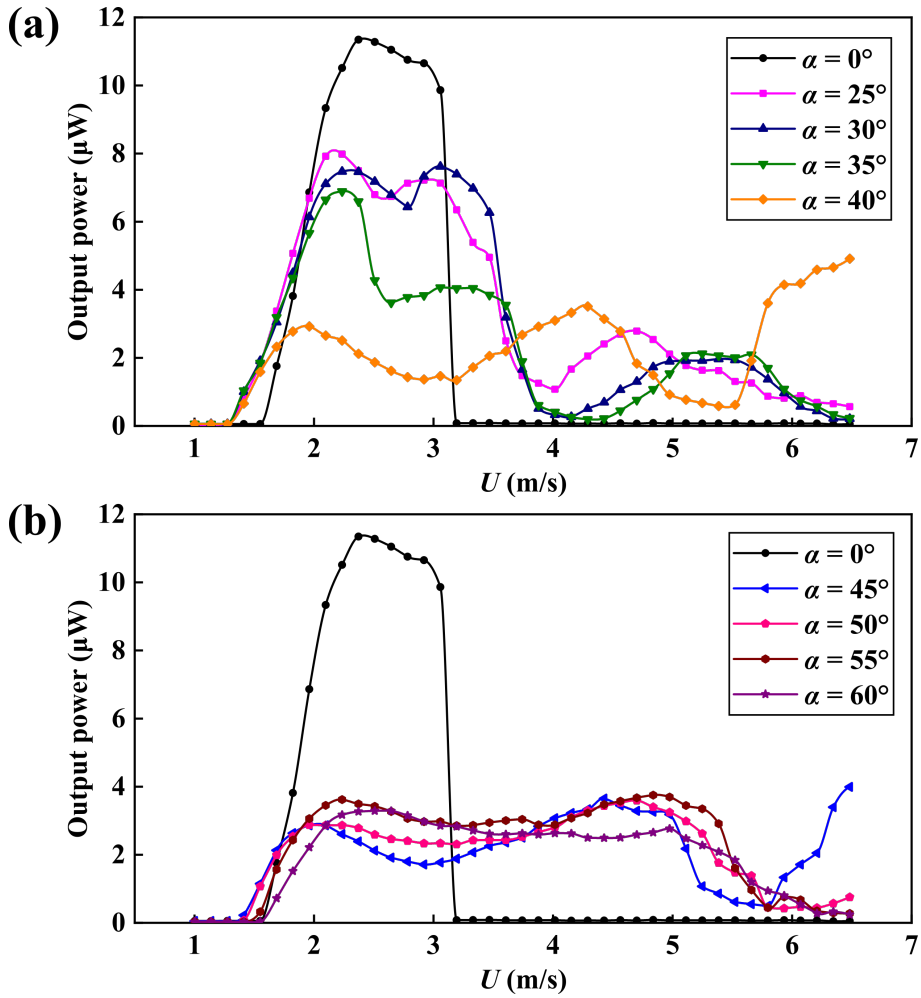

Fig. 15. Variation of the power output against wind speed for different cylinders: (a) cylinders at α = 0°, 25°, 30°, 35° ,40°; (b) cylinders at α = 0°, 45°, 50°, 55° ,60°.

4. Mechanism analysis based on CFD

This section uses three-dimensional CFD simulation results to illustrate the mechanism of torsional vibration and explain the causes of the aforementioned typical experimental results. A series of CFD simulations were conducted in the platform XFlow (Dassault, co.) [35]. The XFlow platform is a platform based on the Lattice-Boltzmann method (LBM), which can realize parallel multi-core computing. In order to better understand the solution process of the LBM, Fig. 16 depicts the flowchart of the CFD simulation solution to show the step-by-step implementation of the method. The Smagorinsky turbulence model of large eddy simulation function providing by XFlow platform is adopted to perform the turbulence simulation. The Smagorinsky turbulence model has reasonable accuracy when calculating aerodynamic characteristics, which can minimize the error of computational and modeling [54,55].

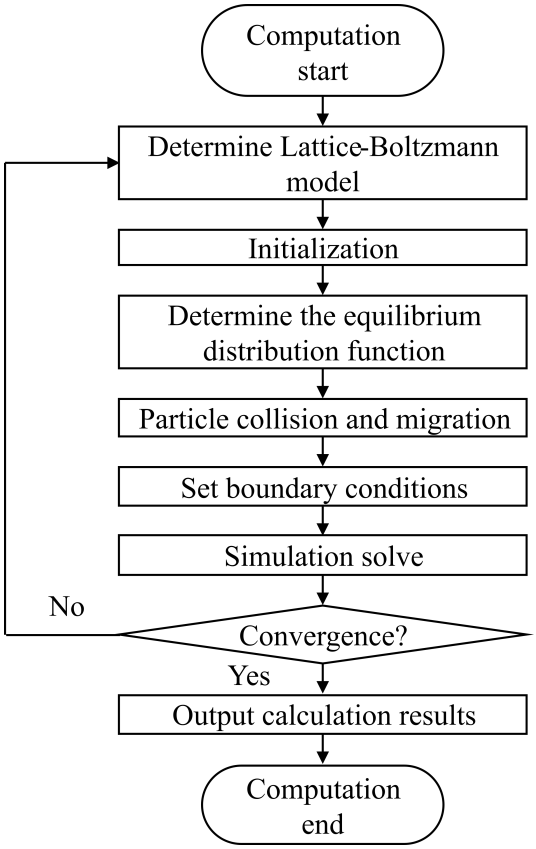

Fig. 16. Flowchart of the simulation solution by Lattice-Boltzmann method (LBM).

Fig. 17(a) – (c) present the vorticity contours of the three selected typical cases obtained from CFD simulations to illustrate the flow patterns around. The simulation calculation time for each case on the Xflow platform is approximately 72 hours with present computational precision and resources. As shown in Fig. 17(a), for the cylinder at $\alpha = 0°$, the wake shape has shown obvious three-dimensional characteristics. However, it can still be observed that the free shear layer on the surface of the cylinder can regularly fall off and form vortices, which will disperse until it is dissolved as the fluid moves downstream. As a result, there is still a regular turbulent vortex street behind the cylinder at $\alpha = 0°$. In Fig. 17(b), compared to the circular cylinder at $\alpha = 0°$, the vortex street behind $\alpha = 30°$ is more chaotic, with only a small number of broken vortices appear at the top, and a large number of strong vortices gather at the bottom of the inclined cylinder. The reason for this phenomenon is the influence of an axial flow proposed by Matsumoto [50]. The axial flow will prevent the free shear layer from falling off at the top of the inclined cylinder, which makes the formation of the vortex more difficult. However, the axial flow will cause a large number of vortices to converge at the bottom of the inclined cylinder at $\alpha = 30°$, and form a more violent continuous vortex shedding than that behind the cylinder at $\alpha = 0°$. Moreover, the stronger vortex

shedding can cause stronger aerodynamic instability, which leads to much a stronger aerodynamic force at the bottom of the inclined cylinder at $\alpha = 30°$ than that at the top. Therefore, compared with the cylinder at $\alpha = 0°$ with balanced forces on the top and bottom ends, the bottom end of the inclined cylinder at $\alpha = 30°$ can generate greater aerodynamic force at a lower wind speed so that the local force excites the vibration of the whole bluff body. As a result, the inclined cylinder at $\alpha = 30°$ has a lower threshold speed compared to $\alpha = 0°$. Meanwhile, the results studied by Shirakasi et al. [40] indicated that the inclination angle will cause a decrease in the frequency of vortex shedding, which will reduce the aerodynamic force received by the inclined cylinder. Therefore, the maximum RMS voltage and displacement of $\alpha = 30°$ are inferior to that of $\alpha = 0°$. It should be noted that at low wind speed, even if the force at the top and bottom of the inclined cylinder at $\alpha = 30°$ is unbalanced, the bluff body still behaves with the transverse bending vibration mode under the restriction of the cantilever structure. However, at high wind speed, when the vortex shedding frequency of the inclined cylinder at $\alpha = 30°$ approaches the torsional natural frequency, the bluff body will break through the restriction of the structure and begin to produce torsional vibrations. As shown in Fig. 17(c), compared with the inclined cylinder at $\alpha = 30°$, the inclined cylinder at $\alpha = 60°$ has a stronger axial flow effect, which makes the fluid along the axial direction strongly mixed and destroys the complete vortex structure, resulting in a more chaotic turbulent vortex street. The vortex intensity at the bottom of the inclined cylinder at $\alpha = 60°$ is significantly lower than that of the cylinder at $\alpha = 30°$. The vortex of the former one is far away from the surface of the bluff body, which cannot provide more atmospheric power for the bluff body and hence the vibration of the cylinder at $\alpha = 60°$ is lower than that at $\alpha = 30°$. Simultaneously, because the aerodynamic force produced by the bottom of the inclined cylinder at $\alpha = 60°$ is small, the torsional vibration cannot be excited within the experimental wind speed range.

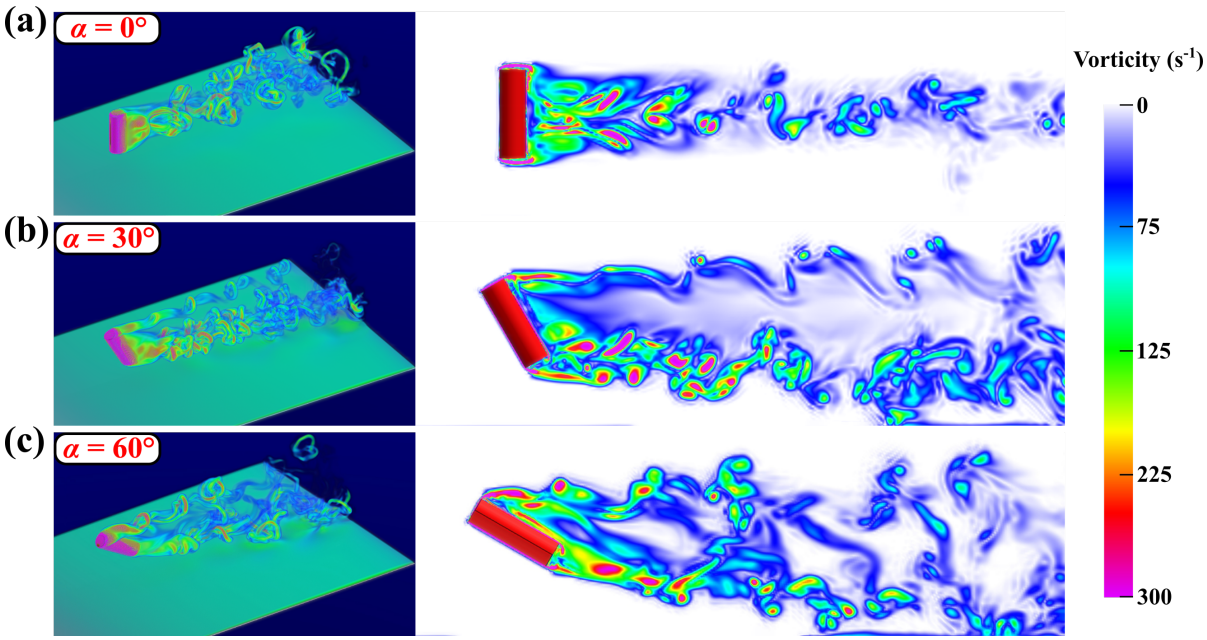

Fig. 17. Vorticity contours of inclined cylinder with different inclination angles obtained from CFD simulation: (a) $\alpha = 0°$, (b) $\alpha = 30°$, and $\alpha = 60°$.

Fig. 18(a) - (c) demonstrate the vorticity vectors of inclined cylinders with different inclination angles to illustrate the near-filed flow around. As can be seen in Fig. 18(a), there are some small spanwise vortices on the back of the cylinder at $\alpha = 0°$, which makes the flow around the cylinder present obvious three-dimensional characteristics. In general, the streamlines along the downstream direction are roughly parallel to each other, and there is no major deviation. In Fig. 18(b), it can be seen that there is an axial vortex (where the streamlines converge) on the backside of the top of the inclined cylinder at $\alpha = 30°$, and all streamlines radiate out after passing through the vortex. One part of the streamline moves to the downstream end in the direction of the cylinder axis, and the other part moves horizontally downstream in the downstream direction. The existence of this axial vortex causes the generation of an axial flow and destroys the free shear layer at the tip of the inclined cylinder, thus destroying the complete vortex structure. In Fig. 18(c), compared to the inclined cylinder at $\alpha = 30°$, the top of the inclined circular cylinder at $\alpha = 60°$ produces a larger axial vortex, which will undoubtedly damage the vortex shedding behind the cylinder to a greater extent. Simultaneously, the streamline is more inclined along the downstream direction, resulting in a stronger axial flow effect.

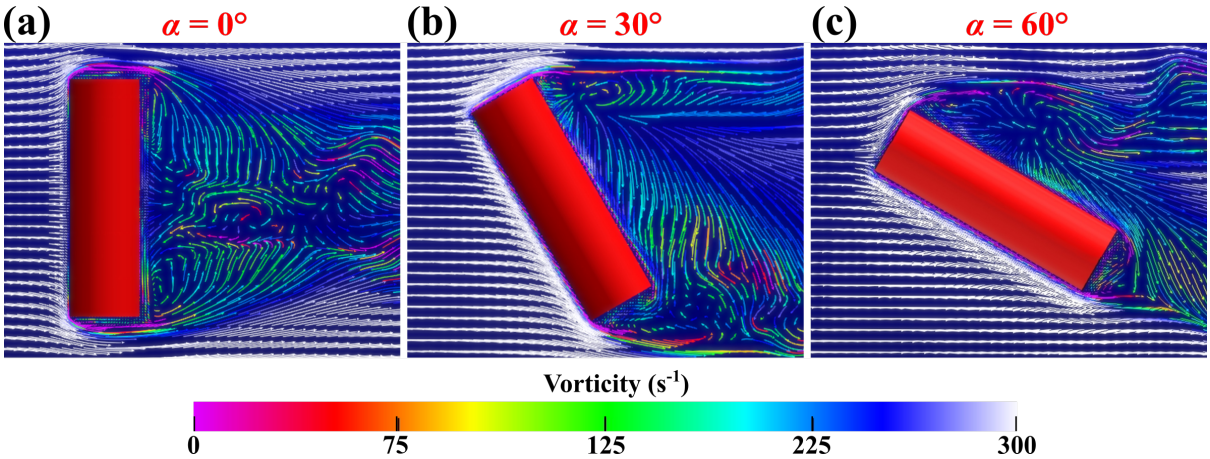

Fig. 18. Vorticity vectors of inclined cylinders with different inclination angles to illustrate the near-filed flow around: (a) $\alpha = 0°$, (b) $\alpha = 30°$, and (c) $\alpha = 60°$.

5. Conclusions

Energy harvesters based on VIV are a classic choice for effectively harvesting wind energy in the environment, and can be used to solve the problem of sustainable power supply for wireless sensors and embedded devices in the environment. It is known that these VIV-based energy harvesters can be deployed in many locations, such as urban high-rises, vents, bridges, rivers, and aircraft structures, etc. However, the conventional VIV-based energy harvester with vertical circular cylinder restricts its development due to its narrow effective wind speed bandwidth. This paper proposed to change the inclination angle α of the circular cylinder relative to oncoming flow to broaden the effective wind speed bandwidth of the VIV-based energy harvester. Wind tunnel experiments were performed to thoroughly investigate the wind speed bandwidth of the energy harvester in terms of the nine different inclination angles α (0°, 25°, 30°, 35°, 40°, 45°, 50°, 55°, 60°). The results showed that compared to the conventional VIVPEH, an appropriate inclined cylinder can significantly broaden the effective wind speed range for the VIVPEH. The inclined cylinder at $\alpha = 60°$ can reduce the threshold wind speed and broaden the effective wind speed bandwidth by more than 229%. Besides, the performance curves of inclined cylinder at 25°, 30°, 35°, 40°, and 45° exhibited two humps within the studied wind speed range. The first hump is the conventional VIV, and the second hump is the coupling of the conventional VIV and torsional vibration. Through dimensionless frequency analysis, it was found that when the threshold wind speed of the torsional vibration was reached, the torsional vibration frequency of the inclined cylinder was close to the torsional natural frequency and then entered a synchronized state. Moreover, the appearance of torsional vibration rapidly reduces the frequency of the conventional transverse VIV, then making

the transverse bending vibration enter the synchronization region again. Finally, the synchronous region of transverse bending vibration and torsional vibration superposed in a certain wind speed range, which causes the voltage to increase rapidly. When α = 50°, 55°, and 60°, the wind speed currently studied cannot induce torsional vibration of the inclined cylinders due to the high torsional natural frequency and the limitation of the structure. The internal mechanisms in the experimental results are further interpreted through comprehensive CFD simulations. The CFD simulations revealed that the existence of an axial vortex downstream of the inclined cylinder led to the generation of an axial flow. The axial flow will prevent the free shear layer from falling from the top of the inclined cylinder and cause a large number of vortices to converge at the bottom, resulting in unbalanced forces at the top and bottom, thus inducing torsional vibration and a series of other phenomena.

It should be mentioned that the energy harvesters with inclined cylinder significantly broaden the wind speed range for harvesting energy, but reduce the power output of the harvesters. The focus of future research is to explore the application of torsional vibration and improve the efficiency of energy harvesters.

Acknowledgments

This work was supported by the National Natural Science Foundation of China (Grant No.: 51977196), China Postdoctoral Science Foundation (2020T130557), Henan Province Science Foundation for Youths (202300410422), and Young Talents of Henan Province (2021HYTP025) .

References

[1] S. Saadon, O. Sidek. A review of vibration-based mems piezoelectric energy harvesters. *Energy Conversion and Management*, 2011, **52**(1): 500-504.

[2] J. Wang, L. Geng, L. Ding, H. Zhu, D. Yurchenko. The state-of-the-art review on energy harvesting from flow-induced vibrations. *Applied Energy*, 2020, **267**: 114902.

[3] J. Wang, Z. Su, H. Li, L. Ding, H. Zhu, O. Gaidai. Imposing a wake effect to improve clean marine energy harvesting by flow-induced vibrations. *Ocean Engineering*, 2020, **208**: 107455.

[4] Z.-Q. Lu, D. Wu, H. Ding, L.-Q. Chen. Vibration isolation and energy harvesting integrated in a stewart platform with high static and low dynamic stiffness. *Applied Mathematical Modelling*, 2021, **89**: 249-267.

[5] X. He, X. Yang, S. Jiang. Enhancement of wind energy harvesting by interaction between vortex-induced vibration and galloping. *Applied Physics Letters*, 2018, **112**(3): 033901.

[6] S. Fang, S. Wang, S. Zhou, Z. Yang, W.-H. Liao. Exploiting the advantages of the centrifugal softening effect in rotational impact energy harvesting. *Applied Physics Letters*, 2020, **116**(6): 063903.

[7] Y. Peng, Z. Xu, M. Wang, Z. Li, J. Peng, J. Luo, S. Xie, H. Pu, Z. Yang. Investigation of frequency-up conversion effect on the performance improvement of stack-based piezoelectric generators. *Renewable Energy*, 2021, **172**: 551-563.

[8] A. Abdelkefi, J. M. Scanlon, E. Mcdowell, M. R. Hajj. Performance enhancement of piezoelectric energy harvesters from wake galloping. *Applied Physics Letters*, 2013, **103**(3): 033903.

[9] A. Abdelkefi. Aeroelastic energy harvesting: A review. *International Journal of Engineering Science*, 2016, **100**: 112-135.

[10] W. Seung, M. K. Gupta, K. Y. Lee, K. S. Shin, J. H. Lee, T. Y. Kim, S. Kim, J. Lin, J. H. Kim, S. W. Kim. Nanopatterned textile-based wearable triboelectric nanogenerator. *Acs Nano*, 2015, **9**(4): 3501-3509.

[11] S. Fang, X. Fu, W.-H. Liao. Asymmetric plucking bistable energy harvester: Modeling and experimental validation. *Journal of Sound and Vibration*, 2019, **459**: 114852.

[12] D. Huang, J. Chen, S. Zhou, X. Fang, W. Li. Response regimes of nonlinear energy harvesters with a resistor-inductor resonant circuit by complexification-averaging method. *Science China Technological Sciences*, 2021, **64**(6): 1212-1227.

[13] F. K. Shaikh, S. Zeadally. Energy harvesting in wireless sensor networks: A comprehensive review. *Renewable & Sustainable Energy Reviews*, 2016, **55**: 1041-1054.

[14] L. Zhao, L. Tang, J. Liang, Y. Yang. Synergy of wind energy harvesting and synchronized switch harvesting interface circuit. *IEEE/ASME Transactions on Mechatronics*, 2017, **22**(2): 1093-1103.

[15] L. Tang, L. Zhao, Y. Yang, E. Lefeuvre. Equivalent circuit representation and analysis of galloping-based wind energy harvesting. *Ieee-Asme Transactions on Mechatronics*, 2015, **20**(2): 834-844.

[16] L. Zhao. Synchronization extension using a bistable galloping oscillator for enhanced power generation from concurrent wind and base vibration. *Applied Physics Letters*, 2020, **116**(5): 053904.

[17] J. Mccarthy, S. Watkins, A. Deivasigamani, S. John. Fluttering energy harvesters in the wind: A review. *Journal of Sound and Vibration*, 2016, **361**: 355-377.

[18] M. Perez, S. Boisseau, M. Geisler, P. Gasnier, J. Willemin, G. Despesse, J. L. Reboud. Aeroelastic flutter energy harvesters self-polarized by triboelectric effects. *Smart Materials and Structures*, 2018, **27**(1): 014003.

[19] B. Zhang, Z. Mao, B. Song, W. Tian, W. Ding. Numerical investigation on viv energy harvesting of four cylinders in close staggered formation. *Ocean Engineering*, 2018, **165**: 55-68.

[20] L. Ding, X. Mao, L. Yang, B. Yan, J. Wang, L. Zhang. Effects of installation position of fin-shaped rods on wind-induced vibration and energy harvesting of aeroelastic energy converter. *Smart Materials and Structures*, 2021, **30**(2): 025026.

[21] L. Ding, Q. Zou, L. Zhang, H. Wang. Research on flow-induced vibration and energy harvesting of three circular cylinders with roughness strips in tandem. *Energies*, 2018, **11**(11): 2977.

[22] Y. Yang, L. Zhao, L. Tang. Comparative study of tip cross-sections for efficient galloping energy harvesting. *Applied Physics Letters*, 2013, **102**(6): 064105.

[23] W. Sun, F. Guo, J. Seok. Development of a novel vibro-wind galloping energy harvester with high power density incorporated with a nested bluff-body structure. *Energy Conversion and Management*, 2019, **197**: 111880.

[24] A. H. Alhadidi, M. F. Daqaq. A broadband bi-stable flow energy harvester based on the wake-galloping phenomenon. *Applied Physics Letters*, 2016, **109**(3): 033904.

[25] C. Zhang, G. Hu, D. Yurchenko, P. Lin, S. Gu, D. Song, H. Peng, J. Wang. Machine learning based prediction of piezoelectric energy harvesting from wake galloping. *Mechanical Systems and Signal Processing*, 2021, **160**: 107876.

[26] S. R. Anton, H. A. Sodano. A review of power harvesting using piezoelectric materials (2003-2006). *Smart Materials and Structures*, 2007, **16**(3): R1.

[27] L.-C. Zhao, H.-X. Zou, Q. Gao, G. Yan, F. Liu, T. Tan, K. Wei, W. Zhang. Magnetically modulated orbit for human motion energy harvesting. *Applied Physics Letters*, 2019, **115**(26): 263902.

[28] G. Chen, L. H. Tang, Z. S. Yang, K. Tao, Z. B. Yu. An electret-based thermoacoustic-electrostatic power generator. *International Journal of Energy Research*, 2020, **44**(3): 2298-2305.

[29] M. Wang, J. Zhang, Y. Tang, J. Li, B. Zhang, E. Liang, Y. Mao, X. Wang. Air-flow-driven triboelectric nanogenerators for self-powered real-time respiratory monitoring. *Acs Nano*, 2018, **12**(6): 6156-6162.

[30] P. K. Sharma, P. V. Baredar. Analysis on piezoelectric energy harvesting small scale device – a review. *Journal of King Saud University - Science*, 2019, **31**(4): 869-877.

[31] H. Zhu, G. Li, J. Wang. Flow-induced vibration of a circular cylinder with splitter plates placed upstream and downstream individually and simultaneously. *Applied Ocean Research*, 2020, **97**: 102084.

[32] Q. Zou, L. Ding, H. Wang, J. Wang, L. Zhang. Two-degree-of-freedom flow-induced vibration of a rotating circular cylinder. *Ocean Engineering*, 2019, **191**: 106505.

[33] J. Wang, G. Hu, Z. Su, G. Li, W. Zhao, L. Tang, L. Zhao. A cross-coupled dual-beam for multi-directional energy harvesting from vortex induced vibrations. *Smart Materials and Structures*, 2019, **28**(12): 12LT02.

[34] W. Sun, S. Jo, J. Seok. Development of the optimal bluff body for wind energy harvesting using the synergetic effect of coupled vortex induced vibration and galloping phenomena. *International Journal of Mechanical Sciences*, 2019, **156**: 435-445.

[35] J. Wang, S. Zhou, Z. Zhang, D. Yurchenko. High-performance piezoelectric wind energy harvester with y-shaped attachments. *Energy Conversion and Management*, 2019, **181**: 645-652.

[36] J. Wang, C. Zhang, S. Gu, K. Yang, H. Li, Y. Lai, D. Yurchenko. Enhancement of low-speed piezoelectric wind energy harvesting by bluff body shapes: Spindle-like and butterfly-like cross-sections. *Aerospace Science and Technology*, 2020, **103**: 10: 105898.

[37] G. Hu, K. T. Tse, K. C. S. Kwok, J. Song, Y. Lyu. Aerodynamic modification to a circular cylinder to enhance the piezoelectric wind energy harvesting. *Applied Physics Letters*, 2016, **109**(19): 193902.

[38] G. Hu, F. Liu, L. Li, C. Li, Y. Xiao, K. C. S. Kwok. Wind energy harvesting performance of tandem circular cylinders with triangular protrusions. *Journal of Fluids and Structures*, 2019, **91**: 102780.

[39] J. Wang, S. Gu, C. Zhang, G. Hu, G. Chen, K. Yang, H. Li, Y. Lai, G. Litak, D. Yurchenko. Hybrid wind energy scavenging by coupling vortex-induced vibrations and galloping. *Energy Conversion and Management*, 2020, **213**: 11: 112835.

[40] L. A. Weinstein, M. R. Cacan, P. M. So, P. K. Wright. Vortex shedding induced energy harvesting from piezoelectric materials in heating, ventilation and air conditioning flows. *Smart Materials and Structures*, 2012, **21**(4): 045003.

[41] G. Hu, K.-T. Tse, K. C. Kwok, J. Song, Y. Lyu. Aerodynamic modification to a circular cylinder to enhance the piezoelectric wind energy harvesting. *Applied Physics Letters*, 2016, **109**(19): 193902.

[42] K. Yang, T. Qiu, J. Wang, L. Tang. Magnet-induced monostable nonlinearity for improving the viv-galloping-coupled wind energy harvesting using combined cross-sectioned bluff body. *Smart Materials and Structures*, 2020, **29**(7): 07lt01.

[43] L. Zhang, A. Abdelkefi, H. Dai, R. Naseer, L. Wang. Design and experimental analysis of broadband energy harvesting from vortex-induced vibrations. *Journal of Sound and Vibration*, 2017, **408**: 210-219.

[44] L. Zhao, H. Zhang, F. Su, Z. Yin, Ieee, *A novel model of piezoelectric-electromagnetic hybrid energy harvester based on vortex-induced vibration*. 2017 international conference on green energy and applications. 2017, New York: Ieee. 105-108.

[45] G. R. Franzini, L. O. Bunzel. A numerical investigation on piezoelectric energy harvesting from vortex-induced vibrations with one and two degrees of freedom. *Journal of Fluids and Structures*, 2018, **77**: 196-212.

[46] Y. Tang, S. Zheng, M. Li. A numerical investigation on galloping of an inclined square cylinder in a smooth flow. *Journal of Wind Engineering and Industrial Aerodynamics*, 2015, **144**: 165-171.

[47] G. Hu, C. Li, K. T. Tse, K. C. S. Kwok. Vortex induced vibration of an inclined finite-length square cylinder. *European Journal of Mechanics B-Fluids*, 2018, **68**: 144-152.

[48] U. Javed, A. Abdelkefi. Role of the galloping force and moment of inertia of inclined square cylinders on the performance of hybrid galloping energy harvesters. *Applied Energy*, 2018, **231**: 259-276.

[49] M. Shirakashi, A. Hasegawa, S. Wakiya. Effect of the secondary flow on karman vortex shedding from a yawed cylinder. *Bulletin of the Japan Society of Mechanical Engineers*, 1986, **29**(250): 1124-8.

[50] M. Matsumoto. Vortex shedding of bluff bodies: A review. *Journal of Fluids and Structures*, 1999, **13**(7): 791-811.

[51] J. D. Hogan, J. W. Hall. The spanwise dependence of vortex-shedding from yawed circular cylinders. *Journal of Pressure Vessel Technology-Transactions of the Asme*, 2010, **132**(3): 031301.

[52] G. R. Franzini, R. T. Goncalves, J. R. Meneghini, A. L. C. Fujarra. Experimental investigation into the flow around a stationary and yawed cylinder under asymmetrical end conditions. *International Journal of Offshore and Polar Engineering*, 2014, **24**(02): 90-97.

[53] A. Khalak, C. H. K. Williamson. Motions, forces and mode transitions in vortex-induced vibrations at low mass-damping. *Journal of Fluids and Structures*, 1999, **13**(7): 813-851.

[54] S. L. Han, R. X. Yu, Z. Y. Li, Y. Y. J. a. M. Wang, Materials. Effect of turbulence model on simulation of vehicle aerodynamic characteristics based on xflow. 2014, **457-458**.

[55] J. Wang, S. Sun, L. Tang, G. Hu, J. L. J. E. Conversion, Management. On the use of metasurface for vortex-induced vibration suppression or energy harvesting. 2021, **235**: 113991.